


# Parameter Design and Study of Microstructure, Mechanical Properties and Permeability of 316L Porous Scaffolds Fabricated by Selective Laser Melting Technology

Xiaoyu Ju<sup>a</sup>, Shubo Xu<sup>a\*</sup> , Xinzhi Hu<sup>a</sup>, Renhui Liu<sup>a</sup>, Kangwei Sun<sup>a</sup>,  
Weihai Zhang<sup>b</sup>, Wenming Wang<sup>c</sup>

<sup>a</sup>Shandong Jianzhu University, School of Materials Science and Engineering, Jinan, 250101, China.

<sup>b</sup>Weifang Fuyuan Supercharger Co., Weifang, 261206, Shandong, China.

<sup>c</sup>Shandong Wenling precision forging Technology Co., Jinan, 271100, Shandong, China.

Received: January 07, 2024; Revised: April 30, 2024; Accepted: May 27, 2024

Structural morphology, defects, compressibility and permeability properties studied by finite element analysis, selective laser melting technology and micromorphology, mainly to analyze the effect of porosity on the performance of porous skeletal scaffolds. The results showed that during the preparation process, there are construction errors. The designed structures were able to meet the requirements of cancellous and cortical bone in terms of compressive stress and elastic modulus. The compressive stresses of the diagonal cubic compact row and octahedron are more similar at the same porosity, the elastic modulus and compressive stress decrease with increasing porosity for three structures. In the hydrodynamic analysis, the maximum flow velocity appears in octahedron up to 0.001m/s. Permeability increases with increasing porosity for all structures. The maximum permeability was obtained at 75% porosity for all structures, the pressure drop for three structures at this porosity was most similar to that of natural bone ( $4.153 \text{ E}^3 \text{ N/m}^3$ ).

**Keywords:** Selective laser melting (SLM), Porous Skeletal Scaffold, Porosity, Finite element simulation (FEM), Permeability.

## 1. Introduction

Bones act as a support for the body and can greatly reduce damage from external impacts<sup>1</sup>. However, there are many examples of bone injuries, in order to solve the problem of difficult to repair bone injuries, artificial bone implants have been discovered and have received widespread attention, the ideal bone implant should have good biocompatibility, excellent bioactivity, and mechanical properties similar to natural bone, etc<sup>2</sup>.

Artificial bone is mainly divided into two categories: dense cortical bone and loose cancellous bone. When choosing bone substitutes, it is necessary to consider whether they can meet the stiffness and strength close to that of natural bone, so as to avoid the generation of “stress shielding” effect. In order to solve the problem of “stress shielding”, which leads to defects such as reduced bone mass and loosening of bone implants, porous skeletal scaffolds have been introduced, and the elastic modulus is reduced by adjusting the size of the porosity of the porous skeletal scaffolds, thus eliminating the “stress shielding” effect<sup>3,4</sup>. At the same time, the pores of the porous skeletal scaffold facilitate the transport and exchange of nutrients, oxygen, cytokines, and other substances in the bone, which promotes the rapid reconstruction of the new bone tissue as well as the osseointegration between the tissue and the implant<sup>5</sup>. Considering the relationship between bone adaptation and mechanical properties, the selection of appropriate pore sizes and geometries has become a major

concern. Numerous studies have shown that porous skeletal scaffolds with a pore size of 400  $\mu\text{m}$  to 700  $\mu\text{m}$  and a porosity of 30% to 95% are more favorable for new bone growth and angiogenesis<sup>6</sup>. Taniguchi et al.<sup>7</sup> noted that scaffolds with pore sizes of 600  $\mu\text{m}$  and 900  $\mu\text{m}$  were more suitable for bone growth than 300  $\mu\text{m}$ . Arjunan et al.<sup>8</sup> systematically investigated the stiffness, strength and stress concentration of scaffolds with different porosities, pointing out that the shape of the pores has an important effect on the permeability, stiffness and strength of the skeleton.

There are many methods to prepare porous skeletal scaffolds, among which the selective laser melting (SLM) technology, as a kind of additive manufacturing, is widely used due to its advantages of manufacturing complex geometries with high precision, more flexible design, shorter production time, various choices of materials, and lower cost<sup>4,9,10</sup>. 316L stainless steel has good biocompatibility and good corrosion resistance, as well as low cost, and has gained a lot of attention because of these advantages<sup>11,12</sup>. Čapek et al.<sup>13</sup> prepared 316L stainless steel scaffolds with 87% porosity similar to the mechanical properties of trabecular bone by the SLM method for replacement of joints with trabecular bone defects.

The current focus of porous scaffold design is mainly on porosity and mechanical properties, neglecting its connectivity, the interconnected apertures can provide sufficient space for cell attachment and growth<sup>14</sup>. Complex internal struts can narrow the connectivity within the structure and stress

\*e-mail: [xsb@sdjzu.edu.cn](mailto:xsb@sdjzu.edu.cn)

concentrations can occur, resulting in cell clogging and affecting cell attachment and growth<sup>15</sup>. According to the study, large bone scaffolds experience cellular wilting, which is caused by insufficient nutrient supply, which means that the distance of nutrient supply to the bone scaffolds under low-mass transportation conditions appears to be 5 mm<sup>16</sup>. The key to successful stent grafting is oxygenation and nutrient transport, and the permeability of the stent is critical in assessing substance transportability<sup>17</sup>. In addition to this, the fatigue resistance of the metal is a critical factor, and porous scaffolds prepared by additive manufacturing are more prone to fatigue damage. Defects in the construction process (porosity, inclusions, unfused, etc.), roughness, etc. can greatly affect the fatigue properties of the material<sup>18</sup>. However, there are relatively few studies related to fatigability, which should be given greater attention.

In this paper, three different structures of 316L stainless steel porous skeletal scaffolds were prepared using SLM technique. Four different porosities were designed for each of these structures, and finite element simulations and related experiments were performed to investigate the effect of porosity of porous skeletal scaffolds on their mechanical properties as well as permeability properties, provide options and theoretical support for optimal porosity and structure applicable to different skeletal parts of the human body.

## 2. Experimental Materials and Sample Preparation

### 2.1. Selection of experimental material

In this paper, the 316L powder obtained by argon atomization method was chosen as the raw material, and the 316L powder was mainly presented as a spherical shape, with the particle size mainly distributed in the range of 6-40 $\mu$ m, and the average particle size was 19.6 $\mu$ m as shown

in Figure 1b, and the distribution of its main elements was shown in Table 1 below.

### 2.2. Sample preparation

#### 2.2.1. Bracket three-dimensional model design

The bracket model was generated by UG 12.0 (Siemens PLM Software, USA). In this paper, body-centered cubic peripheral square (SCBCC), diagonal cubic compact row (DCC) and octahedron (ODC) are selected as the research objects. The SCBCC structure is a transversely isotropic lattice structure that better mimics natural bone properties, maintains physiological load transfer and reduces implant-induced stress-strain deformation<sup>19</sup>. The BCC structure has good controllability of porosity due to its ideal isotropic properties<sup>20</sup>. ODC structures have high modulus of elasticity and yield strength, making them the best choice for lightweight structures<sup>21</sup>. Three types of structural units are shown in Figure 2, the specific modeling process is shown in Figure 3. The theoretical porosity  $P$  of the porous scaffold is shown by the mathematical model Equation 1. Where  $V_1$  is the volume of porous structure and  $V_2$  is the volume of dense structure. The porosity of the scaffold and its pore diameter  $d$  were controlled by setting the cylindrical diameter  $r$  and cylindrical length  $L$  in the modeling. Numerous studies have shown that porous implants with porosities of 30% to 95% exhibit better new bone growth and angiogenesis<sup>6</sup>. The porosity of the scaffold was set to be 55%, 65%, 75%, and 85% in this study, respectively, and the specific design parameters are shown in Table 2. Porous scaffolds with different unit structures are abbreviated by the name of the structure - porosity, e.g. DCC-55%, DCC-65%, DCC-75%, DCC-85%, etc.

$$P = \left( 1 - \frac{V_1}{V_2} \right) \times 100\% \quad (1)$$

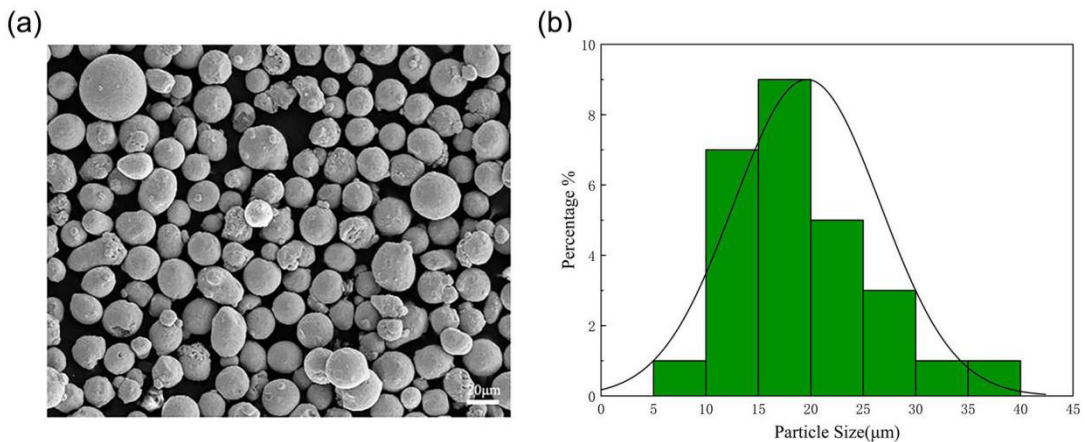


Figure 1. (a) SEM image of 316L powder; (b) particle size distribution.

Table 1. 316L powder element distribution.

Element	Fe	C	Mn	Si	Ni	Cr	Mo	S	P
Content(wt.%)	67.189	0.015	0.90	0.43	10.66	17.49	2.36	0.005	0.020

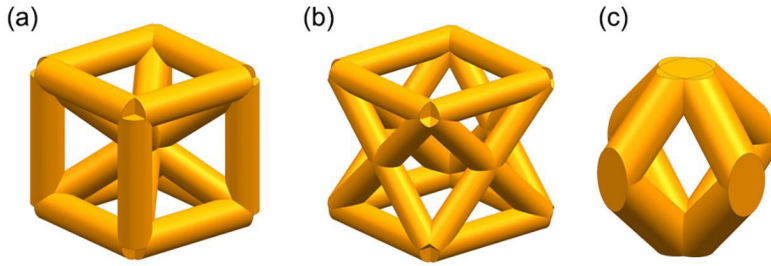


Figure 2. Unitary structure of porous skeletal scaffold (a) SCBCC; (b) DCC; (c) ODC.

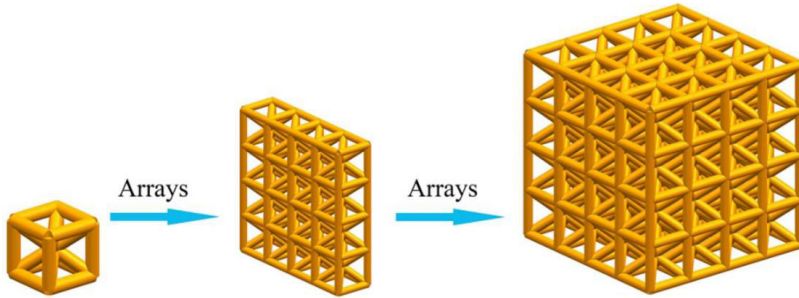


Figure 3. Porous skeletal scaffold modeling steps.

Table 2. Porous skeletal scaffold design parameters.

Structures	Porosity (%)	Cylinder diameter(mm)	Cylinder length (mm)	Pore size (μm)
SCBCC	55	0.58	3.20	250
	65	0.50	3.00	330
	75	0.40	3.10	430
	85	0.30	3.20	530
DCC	55	0.63	2.80	198
	65	0.52	2.80	308
	75	0.43	2.80	398
	85	0.31	2.80	518
ODC	55	0.78	1.70	634
	65	0.66	1.62	754
	75	0.54	1.56	874
	85	0.40	1.42	994

### 2.2.2. Preparation of 316L porous skeletal scaffolds by SLM method

The metal additive manufacturing equipment used in this study is the FS121M metal forming equipment developed independently by China Huashu Hi-Tech, and the forming method is selective laser melting. The 3D model is imported into the machine via a stereolithography (STL) file, then the process parameters are set, and this machine executes along the necessary tool paths based on the imported STL file, building 2D layers directly, each one on top of the previous one, and finally making the 3D part<sup>22</sup>. Among the selected process parameters are laser power 190W, scanning pitch 0.08mm, scanning speed 900mm/s, laying powder thickness 0.03mm, this parameter is the default parameter of the machine, and the energy density can be obtained as 88.96J/mm<sup>3</sup>. Three copies of porous skeletal scaffolds with different structures and different porosities were printed for each group, and the samples are shown in Figure 4.

EDM wire cutting was used to cut the printed experimental parts from the stainless steel plate. The cut experimental parts were put into the ultrasonic cleaning machine, anhydrous ethanol was poured into the ultrasonic cleaning machine until the experimental parts were submerged, ultrasonic cleaning was carried out, and so on for 5~6 times to remove the excess metal powder remaining in the porous skeletal scaffolds, and the experimental parts were taken out for drying and standby.

The test methods mainly include:

1. The samples were finely scanned using a KMS laser spectroscopic confocal microscope and their profiles were measured to derive the error value between the actual porosity and the theoretical porosity.
2. By using WDW-100E electronic universal testing machine, compression experiments were carried out on porous skeletal scaffolds with different structures and different porosities to study their mechanical properties.
3. Finite element simulation of porous skeletal scaffolds was performed using Ansys software. Compression simulation and hydrodynamic simulation of porous skeletal scaffolds were performed using Static Structure module and Fluent module in Ansys software, respectively. In order to improve the computational accuracy and save computational resources, the model is composed of 4×4×4 cells, and the cell mesh is selected to be divided by tetrahedral mesh. The mesh size was optimized by the mesh sensitivity program, taking into account both accuracy and time, and the final mesh size was set to 0.05 mm.
4. The porous scaffolds were characterized by micromorphology (SEM) using a SUPRA 55 scanning electron microscope. Study its structural morphology and defects.



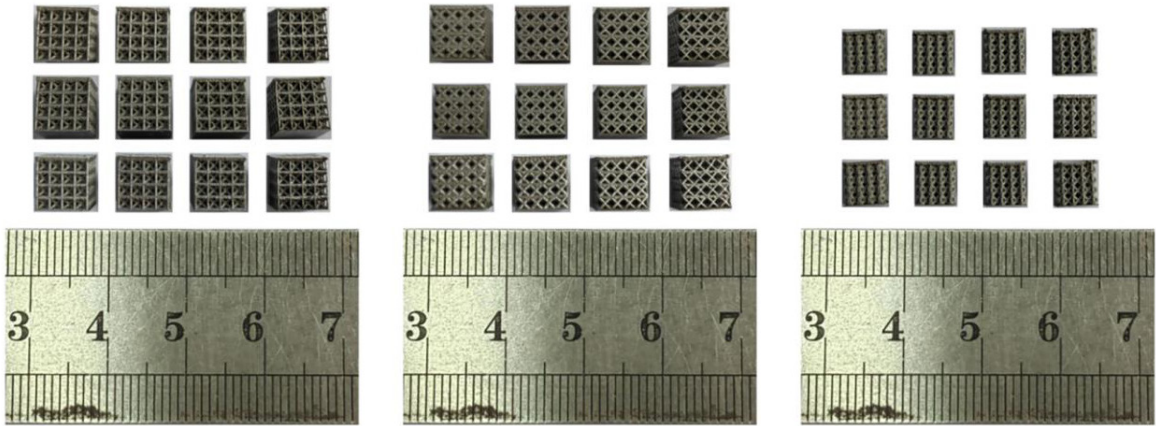


**Figure 4.** SLM-formed porous skeletal scaffolds (a) SCBCC; (b) DCC; (c) ODC.

### 3. Experimentation and Simulation

#### 3.1. Error analysis

The laser power directly affects the energy input to the SLM, producing different defects, which in turn affects the quality of the printed sample. Incomplete melting or spheroidization of powder are two common phenomena, where spheroidization leads to the creation of irregular pores, and incomplete melting of powder leads to the presence of unmelted particles in the melted powder, which combine to create defects<sup>23</sup>. Either case affects the porosity of the porous scaffold, making the actual porosity in error from the theoretical porosity.

The porous skeletal scaffolds were characterized microscopically, and as shown in Figure 5, the internal defects were mainly in the form of irregular circular shaped pore defects (red arrows) and unmelted residue defects (white arrows). The reason for this phenomenon is: As the layers of powder are stacked on top of each other, the powder undergoes continuous melting and cooling to form new layers. Depending on the input energy, when the energy does not reach the required value, the powder fails to fill the pores and irregular pores are formed, accompanied by the adhesion of unmelted powder on the surface. The effects of the defects on the organization and properties of the scaffolds cannot be ignored and subsequent studies are still needed.

As shown in Figure 6, the laser diagrams of three different structures with different porosities, in which the three structures have the same pattern of microscopic contour diameters, all of them have the most severe powder adhesion in the transverse strut and the relatively weakest in the longitudinal strut. There is irregular pore generation inside the strut of the porous stent, and there is more powder adherence around it, in which the particles on the upper surface are more firmly adhered, and the particles on the lower surface are more loosely adhered, which leads to an increase in the diameter of the strut column and affects the porosity. Three structures with a porosity of 75% are used as examples for specific analysis. As shown in Figure 7, all three structures exhibit an increase in the cylindrical diameter



**Figure 5.** Microstructural defects of the stent.

of the struts, and transverse strut diameter > staggered strut diameter > longitudinal strut diameter, resulting in actual porosity < theoretical porosity. The reason for the above phenomenon may be: during the construction process, the heating of SLM technology is accumulated layer by layer, and the new layer is always exposed to the laser beam and the powder is completely melted. Surrounded by unmelted powder, its heat transfer effect is not good, so the heat is mainly dissipated by the solidification of the lower layer. There is no support at the bottom, and the lower surface is directly in contact with the unmelted powder, which is easy to produce overheating phenomenon; therefore, when the melt pool is solidified, the unmelted powder is mainly adhered to the lower surface, which makes the cylindrical diameter of the strut increase and produces errors.

Table 3 shows the error values of three structures with different porosities. As shown in Table 3, the error is controlled from 0.16% to 3.83%, this error is generated at the time of construction, and the process parameters at the time of printing can be adjusted to reduce. The error is within manageable limits and has a negligible effect on the performance of the bracket.

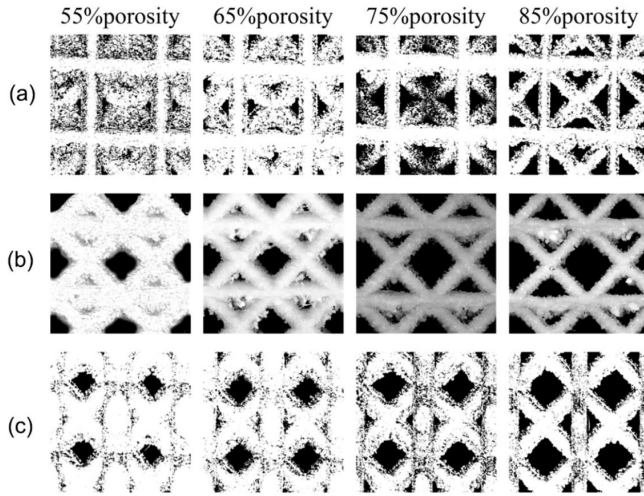


Figure 6. Laser maps of three different structures with different porosities (a) SCBCC; (b) DCC; (c) ODC.

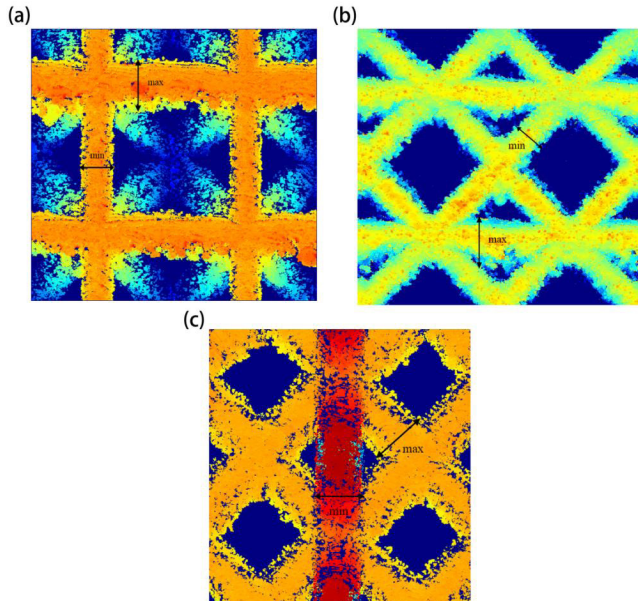


Figure 7. Microcontours of three different structures with 75% porosity (a) SCBCC; (b) DCC; (c) ODC.

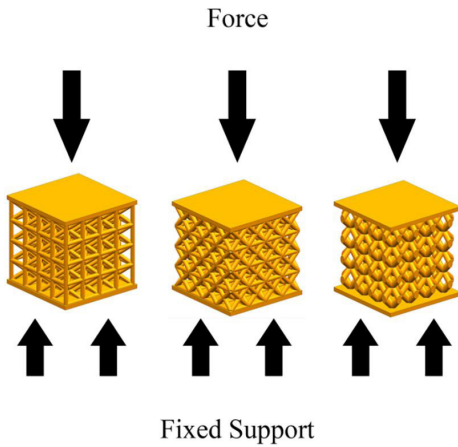
Table 3. Error values of different porosities for three different structures.

Structures	Actual cylinder diameter (mm)	Actual pore size ( $\mu\text{m}$ )	Theoretical porosity(%)	Actual porosity(%)	Errors(%)
SCBCC	0.631	234.94	55	52.50	2.5
	0.526	321.76	65	62.55	2.45
	0.427	419.52	75	73.85	1.15
	0.359	514.12	85	82.51	2.49
DCC	0.684	176.98	55	53.32	1.68
	0.627	283.49	65	62.81	2.19
	0.485	388.65	75	74.13	0.87
	0.462	502.97	85	82.57	2.43
ODC	0.887	600.17	55	51.17	3.83
	0.682	740.72	65	64.84	0.16
	0.573	860.20	75	74.60	0.40
	0.4889	964.15	85	81.45	3.55

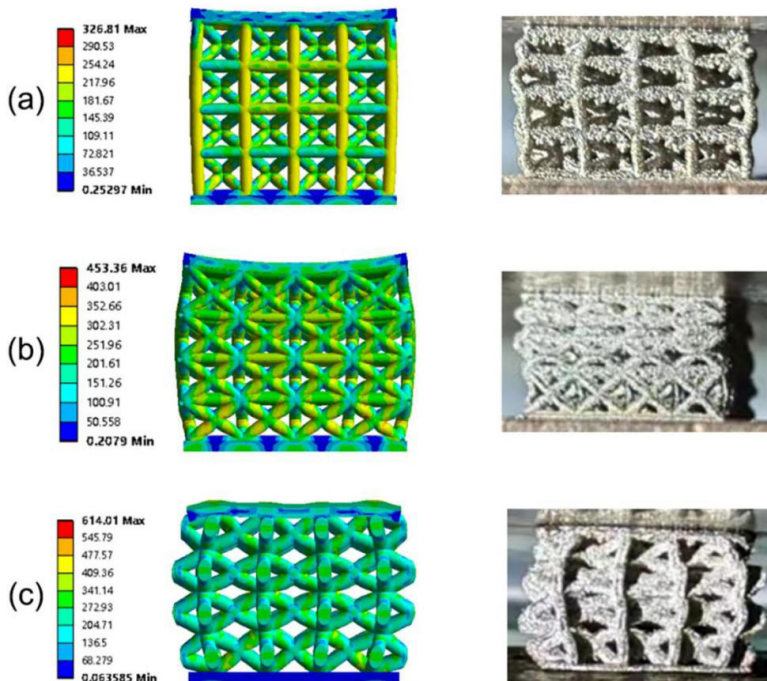
### 3.2. Compressive performance test

#### 3.2.1. Static mechanics

In the finite element analysis, due to the specificity of the three structures, and in order to ensure that the forces on the three structures are uniform during compression, thin plates are added to the top and low ends of the three brackets for compression to simulate the process of their compression. The boundary conditions of the finite element simulation were kept consistent with the experiments, a force with a direction axially downward and a size of 3000 N was applied, with the bottom set as a complete constraint, the compression was carried out with a speed of 1 mm/min during the experiments, and the deformation was stopped when the deformation reached about 70%. The specific design is shown in Figure 8.



**Figure 8.** Static mechanical finite element model diagrams (a) SCBCC; (b) DCC; (c) ODC.



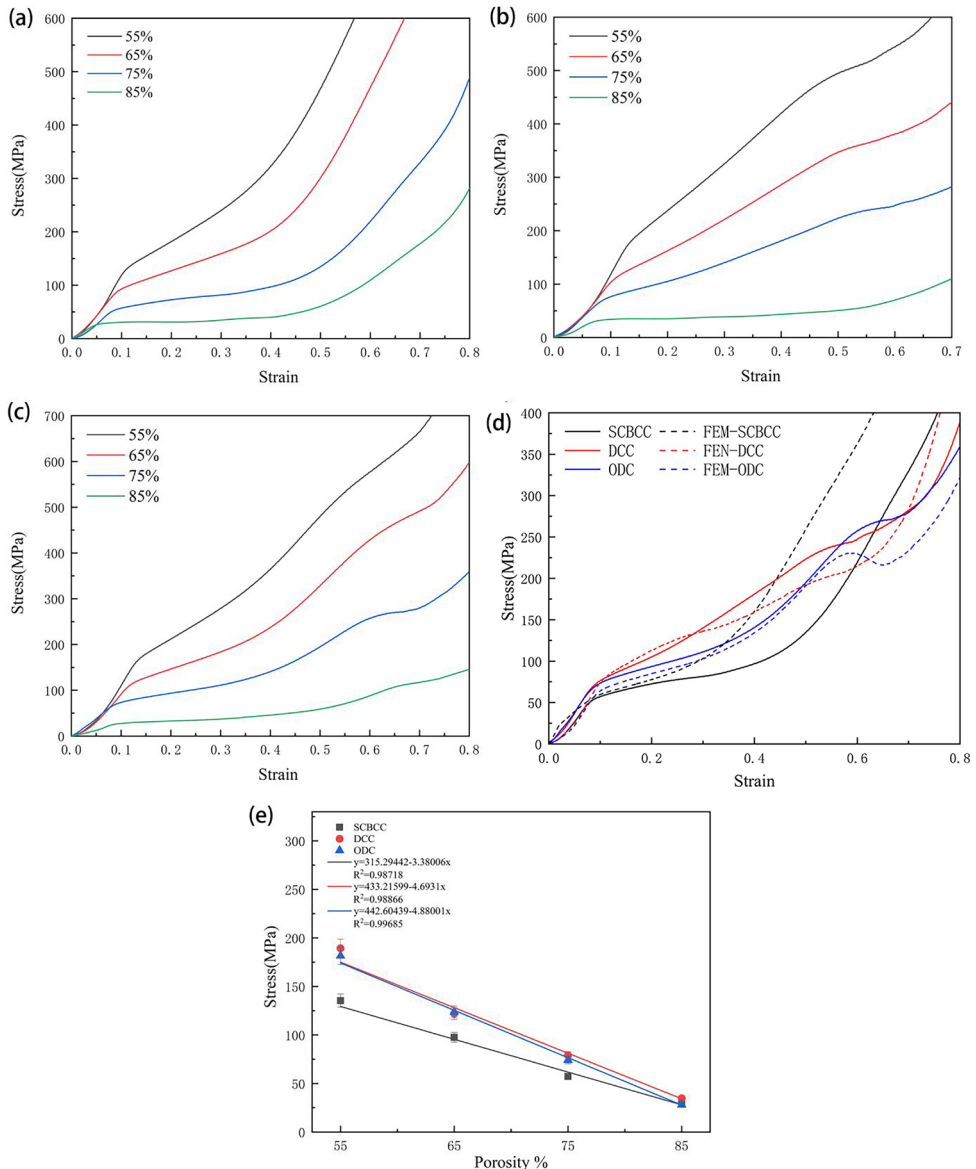
**Figure 9.** Finite element simulation and actual compression of porous skeletal scaffolds (a) SCBCC; (b) DCC; (c) ODC.

Figure 9 shows the finite element simulation and the actual compression of the porous skeletal scaffold. From Figure 9, it can be seen that the deformation of three structures is obvious bending deformation of the cylindrical rod emanating from the center of the unit, and obvious irregular deformation of the enclosed aperture. It can also be seen from the figure that the three structures also have different deformation characteristics. When the Figure 9a (SCBCC) is subjected to compression force, the column part of the unit body mainly acts as a support, the cross-column part is subjected to the smallest force, and in the finite element analysis, it can be clearly seen that the stress concentration occurs at the intersection of the column and the unit columns, in the experimental process, it is also the first deformation that occurs in this part. Figure 9b (DCC), the stress is mainly concentrated on the cross columns, the cross columns at the bottom are subjected to the largest stress, while the intersection of the columns is subjected to the smallest stress, and it can be found in the actual experiments that the deformation is in the way of collapsing layer by layer from the top to the bottom, there is a slight breakage on the cross columns at the lowest end. For the SCBCC and DCC, the internal transverse columns are mainly subjected to compressive shear force, which is mainly used to resist the longitudinal deformation of the columns, so the transverse columns in the two structures are subjected to the smallest force. Finally Figure 9c (ODC) can be seen, in the force, each unit deformation degree is different, the overall deformation trend for the external expansion of deformation, accompanied by the occurrence of the phenomenon of twisted tilt, the stress is concentrated in the bottom periphery of the tilted pillars, so the first deformation occurs. It is basically consistent with the stress distribution, main deformation parts and overall deformation predicted in the finite element.



Figure 10 shows the stress-strain curves for different structures and different porosities. It was found that the compression process of the porous skeletal scaffolds is mainly divided into three stages, which are the elastic stage, the plastic deformation stage and the compaction stage<sup>24</sup>. In the elastic stage, the stress increases linearly with the increase of strain; in the plastic deformation stage, the trend of increasing stress decreases with the increase of strain, and the whole stent produces plastic deformation, the stent continues to deform as the load force continues to increase, so that the stent gradually tends to be densified, which results in the rise of compressive resistance; in the compaction stage, the compressive resistance continues to be improved, and this phenomenon occurs because of the adhesive bonding of the un-melted or semi-melted powder around the central connection point of the unit and the

intersection portion of the unit columns gives the skeletal stent its resistance to buckling. From Figure 10d, it can be seen that the compressive strength of the three structures is DCC>ODC>SCBCC for the same porosity of 75%. The compressive stresses of DCC-75%, ODC-75%, and SCBCC-75% were 78.93 MPa, 74.10 MPa, and 57.24 MPa, respectively. The compressive properties and stress magnitudes are in general agreement with those predicted in the finite elements. Figure 10e is the result of the compressive stress obtained from the stress-strain curve, from (e) it can be seen that the relationship between all three structures and porosity is a linear equation, and the compressive stresses of DCC and ODC are similar with the same porosity, and there is a large difference with SCBCC. The compressive stress decreases with increasing porosity, independent of the structure of the porous scaffold.



**Figure 10.** Stress-strain curves for different structures and different porosities (a) SCBCC; (b) DCC; (c) ODC; (d) Comparison of stress-strain for different structures with a porosity of 75% \ Comparison of testing and simulation of three structures with 75% porosity; (e) Porosity vs. compressive stress.

### 3.2.2. Modulus of elasticity of porous skeletal scaffolds

The magnitude of elastic modulus of a porous skeletal scaffold is the primary prerequisite for measuring whether a porous skeletal scaffold meets the requirements for implantation. For the calculation of elastic modulus of porous parts, the Gibson-Ashby<sup>25</sup> formula is usually used, according to which it can be calculated whether the porous bracket meets the requirements of implantation or not, and the formula is shown below:

$$\frac{E^*}{E_s} = C \left( \frac{\rho^*}{\rho_s} \right)^m \quad (2)$$

Where  $E^*$  is elastic modulus of the porous skeletal scaffold and  $E_s$  is elastic modulus of the solid, 316L stainless steel was chosen as the raw material in this study and  $E_s=210$  GPa,  $\rho^*$  is the density of the porous skeletal scaffold,  $\rho_s$  is the density of the solid 316L stainless steel and  $\rho_s=7.98$  g/cm<sup>3</sup>,  $C$  and  $m$  are the geometrical constants of the porous structure and are taken as  $C=1$  and  $m=2$  respectively.

The actual elastic modulus of the three porous skeletal scaffolds measured after ultrasonic cleaning of the above three structures is shown in Table 4. Figure 11 plots the porosity versus elastic modulus, as shown, the elastic modulus of all the scaffolds conforms to the linear equation, and the order of the elastic modulus of the three structures is ODC>DCC>SCBCC, e.g., the ODC-75%, DCC-75%, and SCBCC-75% of the elastic modulus are 4.7Gpa, 5.6Gpa, and 6.6Gpa, respectively. The elastic modulus decreases with increasing porosity, independent of the structure of the porous scaffold.

The results showed that the compressive stresses of SCBCC, DCC and ODC were 28.70MPa to 135.36MPa, 34.77MPa to 189.32MPa and 28.07MPa to 181.59MPa, respectively; the elastic modulus was 4.1GPa to 5.8GPa,

5.4GPa to 6.8GPa and 6.2Pa to 7.4GPa. The DCC has the highest compressive strength and the ODC has the highest elastic modulus, and both the compressive stress and the elastic modulus are linearly related to the porosity, both decreasing with increasing porosity, independent of the structure of the porous scaffold. Wang et al.<sup>26</sup> proposed the design of braces for orthotropic structures on the outside of body-centered cubic peripheral orthotropic structures, and the measured elastic modulus ranged from 3.4 to 10.6 GPa. Diagonal cubic close-rowed structures (DCC) and octahedral structures (ODC) with elastic modulus ranging from 3.4 GPa to 21.6 GPa were prepared by Volker Weißmann et al.<sup>27</sup> The results of this experiment are similar to those of Wang et al.<sup>26</sup>.

### 3.3. Fluid dynamics analysis

The study of fluid mobility in porous scaffolds can be divided into experimental methods<sup>27-29</sup> and simulation methods<sup>30,31</sup>. Experimental methods can easily measure the permeability of porous scaffolds, but it is difficult to obtain local and microscopic parameters, such as pressure gradients, velocity distributions, etc. Therefore, numerical simulation is more feasible than experimental methods.

In the finite element analysis the object of analysis was considered as an incompressible and constant density fluid, the fluid material chosen during the simulation calculations was Dulbecco's modified Eagle's medium (DMEM). The boundary conditions are set to an inlet velocity  $V_{in} = 0.001$  m/s, corresponding to a flow rate  $Q = 0.96$  ml/min, a density  $\rho = 1000$  kg/m<sup>3</sup> and zero pressure at the output port<sup>32</sup>. The permeability  $K$ <sup>27,29,33</sup> of the porous support is calculated by Darcy's law with the following equation, where  $\mu$  is the dynamic viscosity taking the value of 0.00145 kg/m/s<sup>31</sup>,  $v$  is the fluid flow rate (m/s),  $l$  is the characteristic length (mm), and  $\Delta p$  is the differential pressure (MPa). The hydrodynamic analysis of the stent evaluates the flow velocity, permeability and fluid pressure of the stent, while allowing visual observation of the velocity flow lines inside the stent.

$$k = \frac{u \cdot v \cdot l}{\Delta p} \quad (3)$$

The flow velocity map of the internal profile of the porous structure shown in Figure 12a, is a CFD model showing the profile on which the fluid velocity is displayed. For three structures studied, the velocity field is visualized in profile. As can be seen from the figure, the velocity field of SCBCC is more uniform, with the maximum flow velocity occurring close to the connecting holes on both sides (region R1 in Figure 12b). Unlike SCBCC, the velocity fields of DCC and ODC are extremely inhomogeneous, with the maximum flow velocity of DCC occurring at the connecting holes near the edge of the stent (region R2 in Figure 12c) and a decreasing trend in the fluid velocity from the edge of the stent to the center of the stent. In contrast to ODC, the fluid velocity spreads outward from the center of the bracket and is greatest at the connecting hole near the center (region R3 in Figure 12d). The velocity fields of the different structures show that the flow velocity of the fluid increases when passing through the connecting holes of the bracket and the maximum flow velocity occurs at the smallest connecting hole of ODC (R3), which is 0.001 m/s.

Figure 13 shows the fluid pressure drop versus permeability between porous scaffolds with different porosities, where

**Table 4.** Elastic modulus of porous skeletal scaffolds.

Experimental Programs	55%	65%	75%	85%	
	SCBCC	5.8	5.2	4.7	4.1
Elastic modulus (Gpa)	DCC	6.8	6.4	5.7	5.4
	ODC	7.4	6.8	6.6	6.2

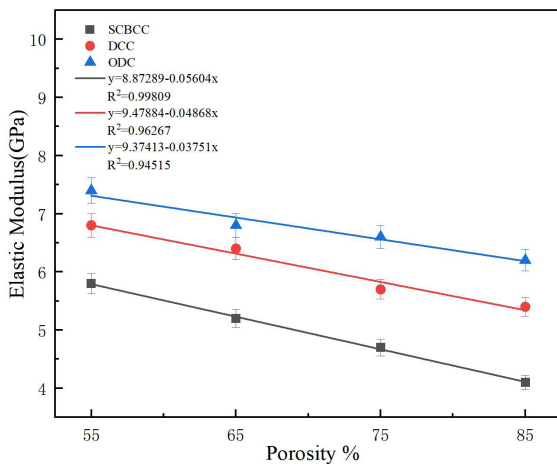


**Figure 11.** Porosity versus elastic modulus.



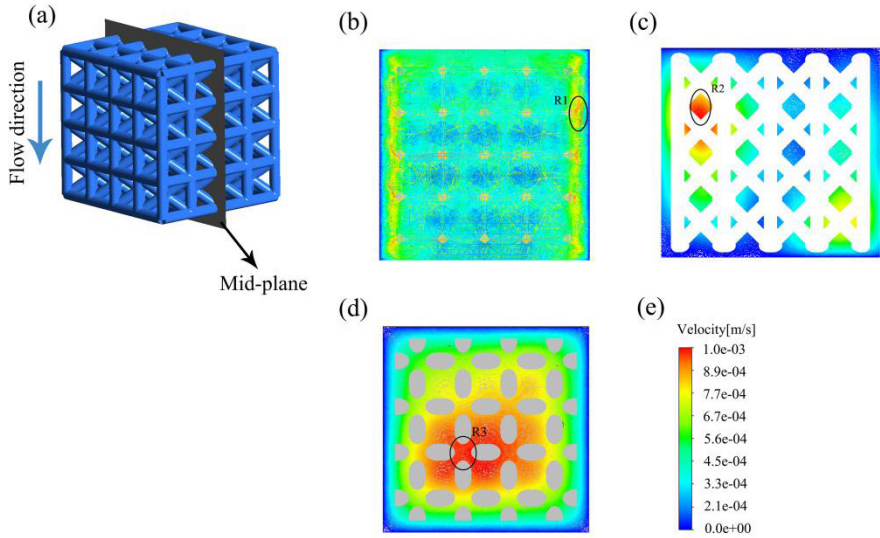


**Figure 12.** Flow velocity maps of internal profiles of porous structures (a) profile CFD model; (b) SCBCC; (c) DCC; (d) ODC; (e) maximum flow velocity scale.

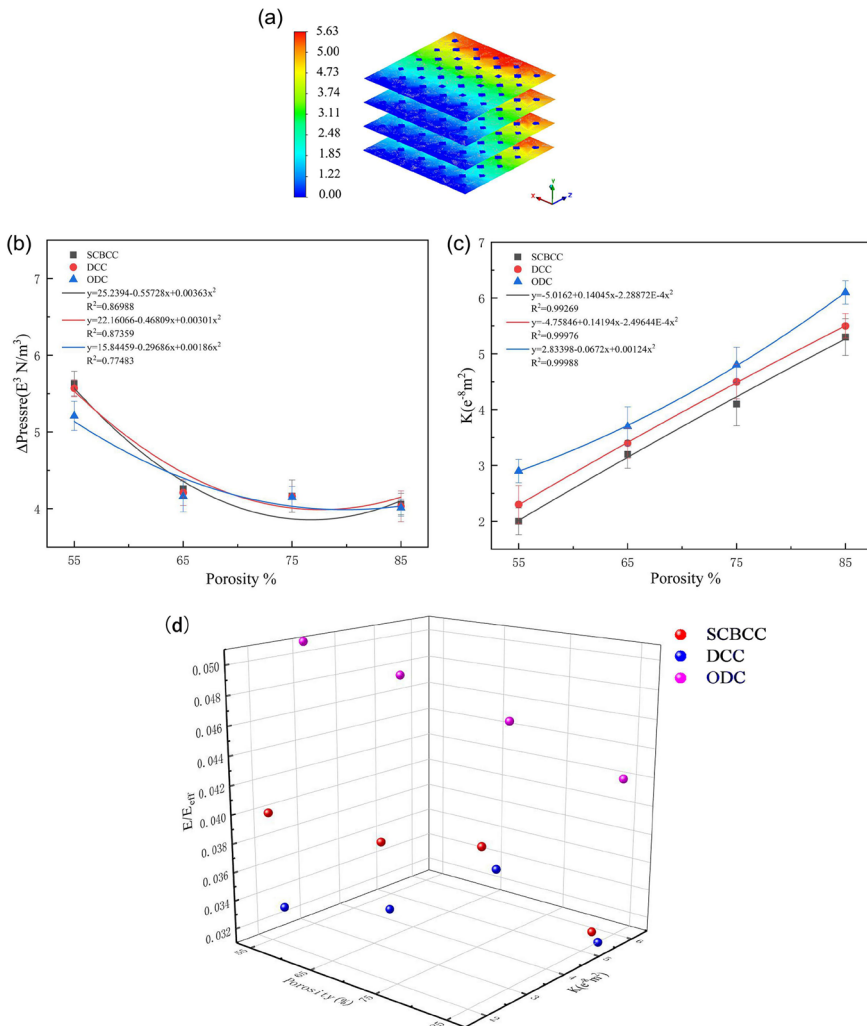


**Figure 13.** (a) Raw pressure gradient plot (SCBCC-55%); (b) fluid pressure drop vs. porosity linear plot; (c) permeability vs. porosity linear plot; (d) Permeability versus stiffness for different structures with different porosities.

(a) shows the original pressure gradient (SCBCC-55%). From Figure 13b, it can be seen that the pressure drop of all three structures shows a decreasing trend with increasing porosity. The pressure drops of SCBCC and DCC were more similar, and ODC had the smallest pressure drop, where the pressure drops of SCBCC-75%, DCC-75% and ODC-75% were  $4.164 \text{ E}^3 \text{ N/m}^3$ ,  $4.161 \text{ E}^3 \text{ N/m}^3$ , and  $4.149 \text{ E}^3 \text{ N/m}^3$ , which is most similar to the pressure drop of natural bone ( $4.153 \text{ E}^3 \text{ N/m}^3$ ). From Figure 13c, it can be seen that the permeability trend is the same for all three structures, which increases with increasing porosity. The ODC has the highest penetration rate and the SCBCC has the lowest penetration rate. The recommended permeability of human bone tissue is approximately  $0.5 \times 10^{-8} < k < 5.0 \times 10^{-8}$  <sup>34-37</sup>, which may result in blockage, metabolic waste and unwanted nutrient transfer through the scaffold when permeability falls below the specified range<sup>8</sup>. Higher permeability is also harmful, causing cells to be flushed affecting the attachment and regeneration of tissue cells<sup>38</sup>. From the figure, it can be seen that SCBCC-85%, DCC-85% and ODC-85% are beyond the range of permeability of human bone tissue, SCBCC-75%, DCC-75% and ODC -75% had the highest permeability of  $4.125 \times 10^{-8} \text{ m}^3$ ,  $4.531 \times 10^{-8} \text{ m}^3$ , and  $4.807 \times 10^{-8} \text{ m}^3$ , respectively. It can be seen that with a porosity of 75%, the designed porous skeletal scaffolds have a rich and diverse local flow structure, which is more conducive to the value-added and differentiation of cells.

The reaction forces are extracted in FEM to calculate the stiffness of the bracket. The formula is shown in 4. where  $E_{\text{eff}}$  is the effective stiffness,  $RF$  is the reaction force, and  $A$  is the total surface area perpendicular to the compression direction. From Figure 13d, it can be seen that the stiffness magnitude of the three structures is ODC>SCBCC>DCC. Permeability and porosity, respectively, tend to be roughly inversely related to stiffness.

$$E_{\text{eff}} = \frac{RF}{A} \quad (4)$$

## 4. Conclusions

In this study, three different structures of 316L stainless steel porous skeletal scaffolds with porosities of 55%, 65%, 75% and 85%, respectively, were prepared using SLM technology. The aim is to reduce the stress shielding effect and to promote osteoclast regeneration and osseointegration. The specific findings are as follows:

1. In the process of SLM construction, due to its layer-by-layer accumulation of heating method and the selection of laser power, the phenomenon of holes and powder particles adherence will occur. Among them, the transverse strut powder adhesion phenomenon is the most serious, mainly manifested in the upper surface of the particles adhered more firmly, the lower surface of the particles adhered more loosely. Generate error, the error is controlled at 0.16%~3.83%.
2. The relationship between compressive stress or elastic modulus and porosity is linear for three structures. The compressive stresses of DCC and ODC are similar for the same porosity, and differ significantly from

those of SCBCC. The magnitude of elastic modulus of the three structures is ODC>DCC>SCBCC. The elastic modulus and compressive stress decrease with increasing porosity for three structures. The compressive stress and elastic modulus of three different structural skeletal scaffolds at four different porosities were able to meet the requirements of cancellous and cortical bone. The test is basically consistent with the compressive performance, stress magnitude and distribution and the main deformation parts and overall deformation predicted in the finite element simulation, which proves the reliability of the finite element simulation, and at the same time, it also provides a reference idea for the development of the porous skeleton scaffold structure.

3. In the evaluation of permeability characteristics, the flow rate of the fluid increases as it passes through the connecting holes of the support. Maximum fluid velocities up to 0.001 m/s occur at the smallest connecting holes in ODC. The maximum permeability was obtained at 75% porosity for three structures, up to  $4.807 \times 10^{-8} \text{ m}^3$ , which is within the range of permeability of human bone tissue and helps to promote nutrient delivery and cell growth after bone implantation. It can be seen that the three structures with a porosity of 75% have the highest cellular value-added efficiency, suggesting that higher permeability helps to promote cell proliferation. The stiffness magnitude of the three structures is ODC>SCBCC>DCC. Permeability and porosity, respectively, tend to be roughly inversely related to stiffness.

In addition to this, fatigue resistance is also a key element of focus. Compared to other mechanical properties, the construction process has the most drastic effect on fatigue properties, and porous structures prepared by additive manufacturing are even more susceptible to fatigue damage. Defects in the construction process (porosity, inclusions, unfused, etc.), roughness, etc. can greatly affect the fatigue properties of the material. The fatigue of the material is directly related to the use of the material quality, service life, etc., can not be ignored, the follow-up need to increase attention.

## 5. Acknowledgments

This study was supported by Natural Science Foundation of Shandong Province (ZR2021ME182), Shandong Province Development and Reform Commission Special Needs Talents Project: R&D and Application of Intelligent Manufacturing Key Technology for High Performance Railway Wheel Unit Production Line (JNGC2023001), State Key Laboratory of Material Forming and Mould Technology Open Fund Project(P12), National Natural Science Foundation of China (52105377) and the Science and Technology Enterprise Innovation Program of Shandong Province, China (2022TSGC2108, 2022TSGC2402, 2023TSGC085, 2023TSGC0119, 2023TSGC0759 and 2023TSGC0961).

## 6. References

1. Cawley DT, Kelly N, Simpkin A, Shannon FJ, McGarry JP. Full and surface tibial cementation in total knee arthroplasty:

- a biomechanical investigation of stress distribution and remodeling in the tibia. *Clin Biomech.* 2012;27(4):390-7. <http://doi.org/10.1016/j.clinbiomech.2011.10.011>.
2. Chen Y, Li W, Zhang C, Wu Z, Liu J. Recent developments of biomaterials for additive manufacturing of bone scaffolds. *Adv Healthc Mater.* 2020;9(23):e2000724. <http://doi.org/10.1002/adhm.202000724>.
  3. Kelly CN, Francovich J, Julmi S, Safranski D, Guldberg RE, Maier HJ, et al. Fatigue behavior of As-built selective laser melted titanium scaffolds with sheet-based gyroid microarchitecture for bone tissue engineering. *Acta Biomater.* 2019;94:610-26. <http://doi.org/10.1016/j.actbio.2019.05.046>.
  4. Wang X, Xu S, Zhou S, Xu W, Leary M, Choong P, et al. Topological design and additive manufacturing of porous metals for bone scaffolds and orthopaedic implants: a review. *Biomaterials.* 2016;83:127-41. <http://doi.org/10.1016/j.biomaterials.2016.01.012>.
  5. Tan XP, Tan YJ, Chow CSL, Tor SB, Yeong WY. Metallic powder-bed based 3D printing of cellular scaffolds for orthopaedic implants: a state-of-the-art review on manufacturing, topological design, mechanical properties and biocompatibility. *Mater Sci Eng C.* 2017;76:1328-43. <http://doi.org/10.1016/j.msec.2017.02.094>.
  6. Wieding J, Lindner T, Bergschmidt P, Bader R. Biomechanical stability of novel mechanically adapted open-porous titanium scaffolds in metatarsal bone defects of sheep. *Biomaterials.* 2015;46:35-47. <http://doi.org/10.1016/j.biomaterials.2014.12.010>.
  7. Taniguchi N, Fujibayashi S, Takemoto M, Sasaki K, Otsuki B, Nakamura T, et al. Effect of pore size on bone ingrowth into porous titanium implants fabricated by additive manufacturing: an in vivo experiment. *Mater Sci Eng C.* 2016;59:690-701. <http://doi.org/10.1016/j.msec.2015.10.069>.
  8. Arjunan A, Demetriou M, Baroutaji A, Wang C. Mechanical performance of highly permeable laser melted Ti6Al4V bone scaffolds. *J Mech Behav Biomed Mater.* 2020;102:103517. <http://doi.org/10.1016/j.jmbm.2019.103517>.
  9. Nandhakumar R, Venkatesan K. A process parameters review on selective laser melting-based additive manufacturing of single and multi-material: microstructure, physical properties, tribological, and surface roughness. *Mater Today Commun.* 2023;35:105538. <http://doi.org/10.1016/j.mtcomm.2023.105538>.
  10. Shi C, Lu N, Qin Y, Liu M, Li H, Li H. Study on mechanical properties and permeability of elliptical porous scaffold based on the SLM manufactured medical Ti6Al4V. *PLoS One.* 2021;16(3):e0247764. <http://doi.org/10.1371/journal.pone.0247764>.
  11. Casati R, Lemke J, Vedani M. Microstructure and fracture behavior of 316L austenitic stainless steel produced by selective laser melting. *J Mater Sci Technol.* 2016;32(8):738-44. <http://doi.org/10.1016/j.jmst.2016.06.016>.
  12. Hermawan H, Dubé D, Mantovani D. Degradable metallic biomaterials: design and development of Fe-Mn alloys for stents. *J Biomed Mater Res A.* 2010;93(1):1-11. <http://doi.org/10.1002/jbm.a.32224>.
  13. Čapek J, Machová M, Fousová M, Kubásek J, Vojtěch D, Fojt J, et al. Highly porous, low elastic modulus 316L stainless steel scaffold prepared by selective laser melting. *Mater Sci Eng C.* 2016;69:631-9. <http://doi.org/10.1016/j.msec.2016.07.027>.
  14. Li S, Kim Y, Choi M, Nam T. Superelastic Ti-18Zr-12.5Nb-2Sn (at.%) alloy scaffolds with high porosity fabricated by fiber metallurgy for biomedical applications. *Intermetallics.* 2019;115:106631. <http://doi.org/10.1016/j.intermet.2019.106631>.
  15. Feng J, Fu J, Yao X, He Y. Triply periodic minimal surface (TPMS) porous structures: from multi-scale design, precise additive manufacturing to multidisciplinary applications. *Int J Extreme Manuf.* 2022;4(2):022001. <http://doi.org/10.1088/2631-7990/ac5be6>.
  16. Maes F, Claessens T, Moesen M, van Oosterwyck H, van Ransbeeck P, Verdonck P. Computational models for wall shear stress estimation in scaffolds: a comparative study of two complete geometries. *J Biomech.* 2012;45(9):1586-92. <http://doi.org/10.1016/j.jbiomech.2012.04.015>.
  17. Kou X, Tan ST. Tan s t. A simple and effective geometric representation for irregular porous structure modeling. *Comput Aided Des.* 2010;42(10):930-41. <http://doi.org/10.1016/j.cad.2010.06.006>.
  18. Benedetti M, du Plessis A, Ritchie RO, Dallago M, Razavi N, Berto F. Architected cellular materials: a review on their mechanical properties towards fatigue-tolerant design and fabrication. *Mater Sci Eng Rep.* 2021;144:100606. <http://doi.org/10.1016/j.mser.2021.100606>.
  19. Alaña M, Lopez-Arancibia A, Ghouse S, Rodriguez-Florez N, Ruiz de Galarreta S. Additively manufactured lattice structures with controlled transverse isotropy for orthopedic porous implants. *Comput Biol Med.* 2022;150:105761. <http://doi.org/10.1016/j.combiomed.2022.105761>.
  20. Luxner MH, Stampfl J, Pettermann HE. Numerical simulations of 3D open cell structures - influence of structural irregularities on elasto-plasticity and deformation localization. *Int J Solids Struct.* 2007;44(9):2990-3003. <http://doi.org/10.1016/j.ijsolstr.2006.08.039>.
  21. Elsayed MSA, Pasini D. Multiscale structural design of columns made of regular octet-truss lattice material. *Int J Solids Struct.* 2010;47(14-15):1764-74. <http://doi.org/10.1016/j.ijsolstr.2010.03.003>.
  22. Mondal P, Das A, Wazeer A, Karmakar A. Biomedical porous scaffold fabrication using additive manufacturing technique: porosity, surface roughness and process parameters optimization. *I J Lightweight Mater Manuf.* 2022;5(3):384-96. <http://doi.org/10.1016/j.ijlmm.2022.04.005>.
  23. Liverani E, Toschi S, Ceschini L, Fortunato A. Effect of selective laser melting (SLM) process parameters on microstructure and mechanical properties of 316L austenitic stainless steel. *J Mater Process Technol.* 2017;249:255-63. <http://doi.org/10.1016/j.jmatprotec.2017.05.042>.
  24. Han C, Yan C, Wen S, Xu T, Li S, Liu J, et al. Effects of the unit cell topology on the compression properties of porous Co-Cr scaffolds fabricated via selective laser melting. *Rapid Prototyping J.* 2017;23(1):16-27. <http://doi.org/10.1108/RPJ-08-2015-0114>.
  25. Li J, Zhang Z-Y, Liu H, Wang Y-B. Design and characterization of novel bi-directional auxetic cubic and cylindrical metamaterials. *Compos Struct.* 2022;299:116015. <http://doi.org/10.1016/j.compstruct.2022.116015>.
  26. Wang L, Kang J, Sun C, Li D, Cao Y, Jin Z. Mapping porous microstructures to yield desired mechanical properties for application in 3D printed bone scaffolds and orthopaedic implants. *Mater Des.* 2017;133:62-8. <http://doi.org/10.1016/j.matdes.2017.07.021>.
  27. Truscello S, Kerckhofs G, van Bael S, Pyka G, Schrooten J, van Oosterwyck H. Prediction of permeability of regular scaffolds for skeletal tissue engineering: a combined computational and experimental study. *Acta Biomater.* 2012;8(4):1648-58. <http://doi.org/10.1016/j.actbio.2011.12.021>.
  28. Lv J, Jia Z, Li J, Wang Y, Yang J, Xiu P, et al. Electron beam melting fabrication of porous Ti6Al4V Scaffolds: cytocompatibility and osteogenesis. *Adv Eng Mater.* 2015;17(9):1391-8. <http://doi.org/10.1002/adem.201400508>.
  29. Cardoso L, Fritton SP, Gailani G, Benalla M, Cowin SC. Advances in assessment of bone porosity, permeability and interstitial fluid flow. *J Biomech.* 2013;46(2):253-65. <http://doi.org/10.1016/j.jbiomech.2012.10.025>.
  30. Deng F, Liu L, Li Z, Liu J. 3D printed Ti6Al4V bone scaffolds with different pore structure effects on bone ingrowth. *J Biol Eng.* 2021;15(1):4. <http://doi.org/10.1186/s13036-021-00255-8>.

31. Chao L, He Y, Gu J, Xie D, Yang Y, Shen L, et al. Design of porous structure based on the Voronoi diagram and stress line for better stress shielding relief and permeability. *J Mater Res Technol.* 2023;25:1719-34. <http://doi.org/10.1016/j.jmrt.2023.05.282>.
32. Olivares AL, Marsal E, Planell JA, Lacroix D. Finite element study of scaffold architecture design and culture conditions for tissue engineering. *Biomaterials.* 2009;30(30):6142-9. <http://doi.org/10.1016/j.biomaterials.2009.07.041>.
33. Dias MR, Guedes JM, Flanagan CL, Hollister SJ, Fernandes PR. Optimization of scaffold design for bone tissue engineering: a computational and experimental study. *Med Eng Phys.* 2014;36(4):448-57. <http://doi.org/10.1016/j.medengphy.2014.02.010>.
34. Dias MR, Fernandes PR, Guedes JM, Hollister SJ. Permeability analysis of scaffolds for bone tissue engineering. *J Biomech.* 2012;45(6):938-44. <http://doi.org/10.1016/j.jbiomech.2012.01.019>.
35. Gómez S, Vlad MD, López J, Fernández E. Design and properties of 3D scaffolds for bone tissue engineering. *Acta Biomater.* 2016;42:341-50. <http://doi.org/10.1016/j.actbio.2016.06.032>.
36. Gonçalves Coelho P, Rui Fernandes P, Carriço Rodrigues H. Multiscale modeling of bone tissue with surface and permeability control. *J Biomech.* 2011;44(2):321-9. <http://doi.org/10.1016/j.jbiomech.2010.10.007>.
37. Syahrom A, Abdul Kadir MR, Abdullah J, Öchsner A. Permeability studies of artificial and natural cancellous bone structures. *Med Eng Phys.* 2013;35(6):792-9. <http://doi.org/10.1016/j.medengphy.2012.08.011>.
38. Emami A, Talaei-Khozani T, Vojdani Z, Zarei fard N. Comparative assessment of the efficiency of various decellularization agents for bone tissue engineering. *J Biomed Mater Res B Appl Biomater.* 2021;109(1):19-32. <http://doi.org/10.1002/jbm.b.34677>.